Aerodynamics: turning wind into mechanical motion

Chapter 1 in IET book "Wind Power Modelling: Atmosphere and Wind Plant Flow" edited by Paul Veers, 2019
Martin O.L.Hansen
DTU Wind Energy

1. Introduction
The aim of a wind turbine is to transform the kinetic energy in the wind into electrical power. The kinetic energy per time [W] that passes an area, A, perpendicular to the wind velocity is

$$P_{avail} = \tfrac{1}{2}\rho V_o^3 A ,\qquad\qquad\qquad\qquad (1.1)$$

(V_o denotes the wind speed and ρ the air density) and the available aerodynamic efficiency is thus naturally defined as the fraction of the actual produced power to the available power in the so called power coefficient

$$C_p = \frac{P}{\tfrac{1}{2}\rho V_o^3 A} . \qquad\qquad\qquad (1.2)$$

To remove kinetic energy from the wind it is necessary to design a rotor that produces an upstream force, denoted the thrust T, which reduces the wind speed behind the rotor, as sketched in Figure 1.1. The wind speed through the rotor is gradually reduced from far upstream, V_o, to, u, at the rotor plane and finally to u_1 in the wake. Due to conservation of mass the streamlines that divide the airflow going through the rotor from the one passing are expanding as drawn in Figure 1.1.
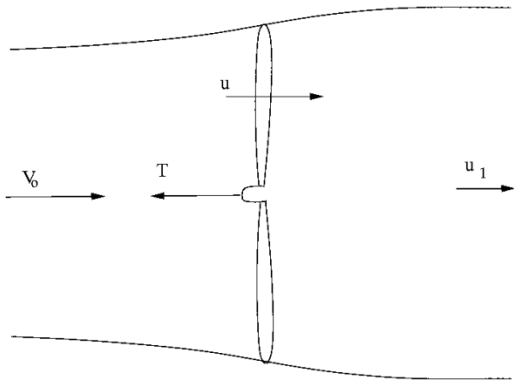

Figure 1.1: A sketch of the overall flow through a wind turbine rotor showing the gradual decrease in wind speed and the associated expanding wake.

In order to transform the extracted power into useful work and not simply dissipate it into internal heat a mechanical torque should also be produced by the rotor as input to the shaft of an electrical generator. In Figure 1.2 is sketched how the aerodynamic loads produce a normal load on the blades to reduce the wind speed and at the same time a tangential load to drive a generator.
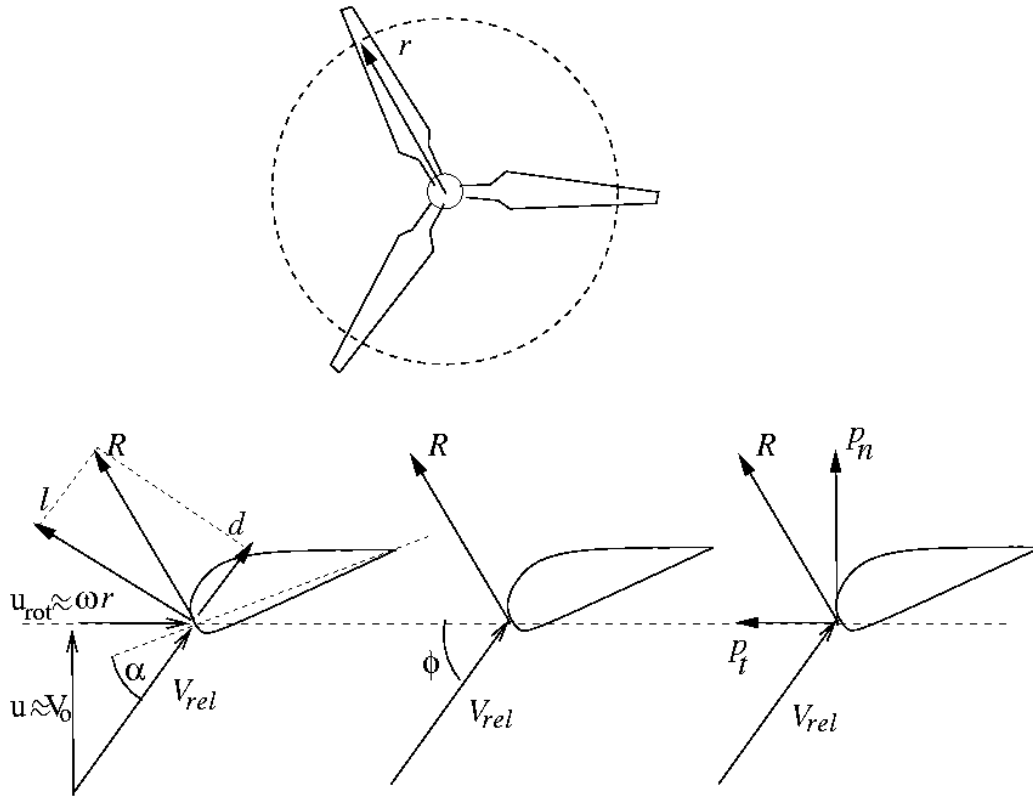

Figure 1.2: A sketch of the rotor, the inflow and aerodynamic loads at a radial cut indicated by the dashed line.

The lower part of Figure 1.2 shows that the cross sections of the rotating blades are shaped as aerofoils and that the approaching relative wind speed, V_{rel}, comes in at an angle of attack, α, to the aerofoils producing a resulting aerodynamic load, R, that has a normal, p_n, and tangential component, p_t, as drawn on the lower right sketch on Figure 1.2. The relative wind is here assumed to be comprised only by the incoming free wind speed and the rotational velocity of the section shown, where in reality there is also a reaction on the incoming air from the aerodynamic loads, known as the induced velocity and that for simplicity has been neglected in Figure 1.2. The normal component of the aerodynamic load, p_n, is responsible for generating the necessary thrust force to reduce the kinetic energy of the wind and the tangential component, p_t, gives the shaft torque needed to extract useful power through an electric generator. Now that the working of a wind turbine rotor has been qualitatively explained the next many following pages will show how the extracted power as function of the free wind speed, the rotational speed and the geometry of the rotor blades can be calculated.

The starting point dates back to the early days of ship propellers where Froude [1] and Rankine [2] developed the very basic momentum theory for an ideal rotor and that is an important part in the popular Blade Element Momentum to be introduced later. Here the flow is considered 1-D , i.e. the wind speed and pressure is assumed to only change in the flow direction and is thus constant with the radius. Further, the flow is considered ideal so that no mechanical energy is lost as heat and under these assumptions the conservation of energy can easily be evaluated on a control volume as the one shown in Figure 1.3. Far upstream the pressure is the ambient pressure p_o and increases with decreasing wind speed downstream to a value p^+ just before the rotor. When passing the rotor the pressure drops Δp and afterwards it gradually increases to the ambient value when the streamlines again becomes parallel.
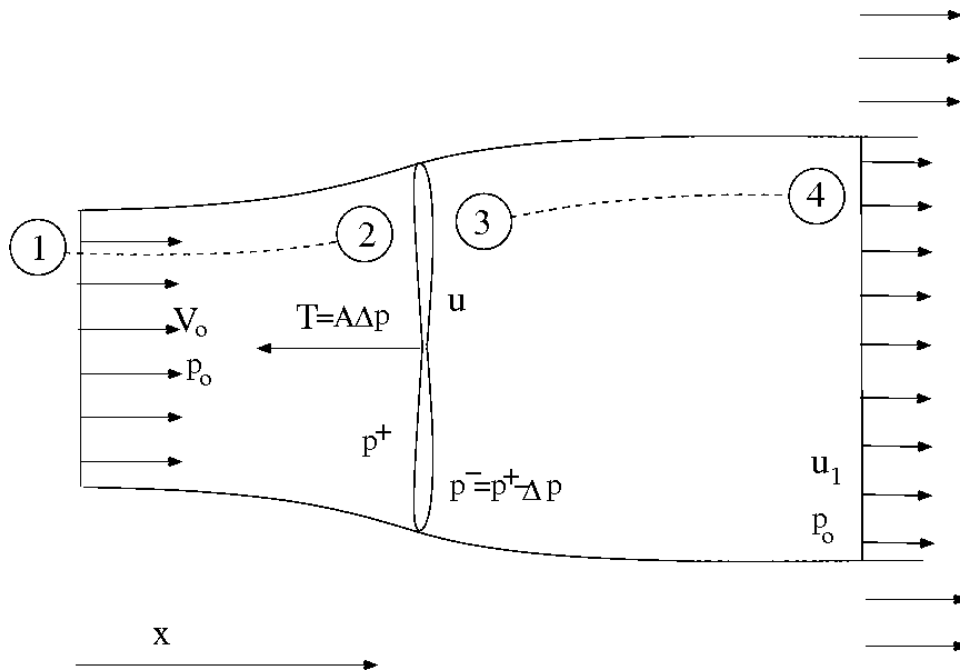

Figure 1.3: Control volume to evaluate the conservation of energy

The lateral side of the control volume in Figure 1.3 follows the streamlines that confine the flow going through the rotor and thus energy is only leaving and entering the control volume at the two vertical end planes and since the pressure at these planes are the ambient pressure the conservation of energy becomes, where P is the power extracted from the flow

$$P = \tfrac{1}{2}\dot{m}(V_o^2 - u_1^2) = \tfrac{1}{2}\rho u A(V_o^2 - u_1^2) \qquad (1.3)$$

The mass flow is constant at any downstream plane from the inlet to the outlet and can be evaluated at the rotor plane where the cross sectional area, A, is known. Since the streamlines that confine the rotor are expanding the local pressure force on the lateral control volume boundary may give a small axial component and by assuming a small expansion one can neglect this contribution to the axial force acting on the control

volume in Figure 1.3 and the only axial force left is the thrust and the evaluation of the axial momentum equation then simply becomes

$$T = \dot{m}(V_o - u_1) = \rho u A(V_o - u_1).$$
(1.4)

The thrust force is created from the pressure jump across the rotor as

$$T = A\Delta p.$$
(1.5)

And since the flow is incompressible, steady and no heat loss is assumed this pressure jump may be evaluated by using the Bernoulli equation from 1 to 2 and again from 3 and 4 shown in Figure 1.3

$$\left. \begin{array}{l} p_o + \frac{1}{2}V_o^2 = p^+ + \frac{1}{2}\rho u^2 \\ p^+ - \Delta p + \frac{1}{2}\rho u^2 = p_o + \frac{1}{2}\rho u_1^2 \end{array} \right\} \Rightarrow \Delta p = \frac{1}{2}\rho(V_o^2 - u_1^2)$$
(1.6)

Combining Eqs. (1.4)-(1.6) it is seen that (for low wake expansion) the wind speed at the rotor plane is the mean of the free wind speed and the wake speed

$$u = \frac{1}{2}(V_o + u_1)$$
(1.7)

Now the axial induction factor, a, is introduced as the non-dimensionalized reduced wind speed at the rotor plane as

$$u = V_o - aV_o = (1-a)V_o$$
(1.8)

Using this definition together with the result in Eq. (1.7) the wind speed in the wake may be written as

$$u_1 = (1-2a)V_o$$
(1.9)

Now putting the expressions (1.8) and (1.9) into Eqs. (1.3) and (1.4) yields

$$P = 2\rho Aa(1-a)^2 V_o^3$$
(1.10)

and

$$T = 2\rho Aa(1-a)V_o^2$$
(1.11)

Using the definition for the power coefficient in Eq. (1.2) and introducing a thrust coefficient as

$$C_T = \frac{T}{\frac{1}{2}\rho V_o^2 A}$$
(1.12)

yields for a 1-D ideal rotor the following relationships

$$C_p = 4a(1-a)^2 \qquad\qquad\qquad\qquad\qquad (1.13)$$

and

$$C_T = 4a(1-a) \qquad\qquad\qquad\qquad\qquad (1.14)$$

It can easily be seen that there is a theoretical maximum value for C_p at 16/27≈0.59 at a=1/3 known as the Betz limit occurring at a non-dimensionalized thrust of C_T=8/9. Now a more in depth understanding of the obtainable values for the power coefficient and the corresponding thrust force and wind speed reduction has been achieved, but still these equations are not detailed enough to analyse a given wind turbine construction nor can they be used in designing an efficient rotor. However, by generalising these equations and combing with the local load production at the rotor blades Glauert [3] derived the very important Blade Element Momentum method that will be shown in the next chapter.

2. Steady Blade Element Momentum method

Glauert [3] combined the momentum theory as described in section 1 with the so called blade element theory from Drzewiecki [4] and derived an algorithm often denoted BEM as an abbreviation for Blade Element Momentum method and that under certain assumptions can be used to compute the performance of an airplane propeller, a helicopter or a wind turbine rotor. First, the classical 1-D momentum theory is assumed to be valid for a local strip on the rotor as shown in Figure 2.1 and that each strip can be treated independently.
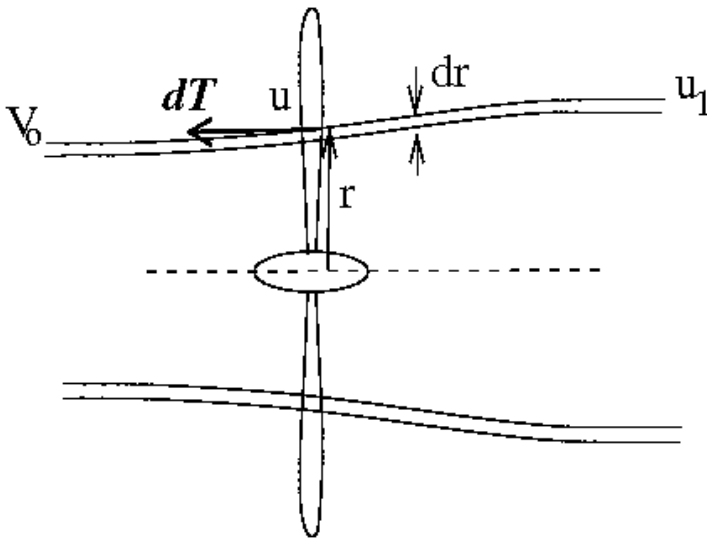

Figure 2.1: A local strip (stream tube) with height, *dr*, passing the rotor

Secondly, in order to be able evaluate the momentum equations (axial and angular), the loads exerted by the rotor on the flow through the strip is assumed not to vary azimuthally corresponding to an infinite number of blades. Under these assumptions the axial momentum equation gives following simple expression for the local thrust force, where the mass flow has been evaluated at the rotor plane and the definition of the axial induction used

$$dT = d\dot{m}(V_o - u_1) = \rho u 2\pi r dr(V_o - u_1) = 4\pi \rho r a(1-a)V_o^2 dr \qquad (2.1)$$

Another expression for the thrust force can be derived applying the so called blade element theory, which is best described with the so called velocity triangle as shown in Figure 2.2 and that shows that the local inflow to the blade, described as a length V_{rel} and an angle with rotor plane, ϕ, is the vector sum of the wind velocity, the relative velocity due to blade rotation and an induced wind, W, which is the reaction on the incoming air from the blade loads. It is seen that the local flow is the 2-D flow past an aerofoil at an angle of attack, α, and where the lift and drag by definition are respectively perpendicular and parallel to the incoming velocity.
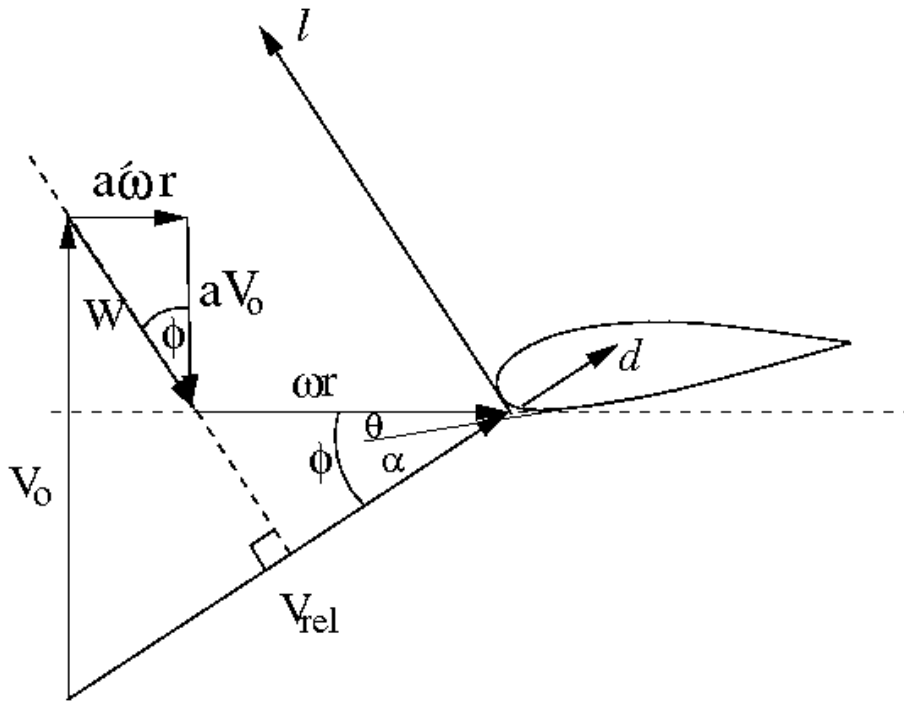

Figure 2.2: The velocity triangle

The dimension of l and d is [N/m] and the force at the strip can be found by multiplying with the number of blades and the length of the blades within the strip, dr. Since the local flow past the blades can be considered

as flow past an aerofoil, the lift and drag can be evaluated from the 2-D lift and drag coefficients, $C_l(\alpha,\text{Re})$ and $C_d(\alpha,\text{Re})$ as

$$l = \tfrac{1}{2}\rho V_{rel}^2 c C_l(\alpha,\text{Re})$$
$$d = \tfrac{1}{2}\rho V_{rel}^2 c C_d(\alpha,\text{Re})$$

(2.2)

provided that these are known for the particular aerofoil as function of angle of attack and local Reynolds number. c is the length of the aerofoil and denoted the chord. The thrust force acting on the strip can thus in the blade element theory be expressed as

$$dT = B(l\cos\phi + d\sin\phi)dr = B\tfrac{1}{2}\rho V_{rel}^2 c(C_l\cos\phi + C_d\sin\phi)dr$$

(2.3)

Combining Eqs. (2.1) and (2.3) one can derive the classical result for the axial induction factor from Glauert [3]

$$a = \frac{1}{\dfrac{4\sin^2\phi}{\sigma C_n}+1}$$

(2.4)

where $C_n = C_l\cos\phi + C_d\sin\phi$ and σ the solidity defined as $\sigma = \dfrac{Bc}{2\pi r}$

Similarly one can derive two equations for the torque exerted on the rotor by the aerodynamic loads

$$dM = \dot{m}rC_{\theta,1} = \rho u 2\pi r dr r C_{\theta,1} \quad \text{(angular momentum equation)}$$

(2.5)

and

$$dM = Brp_t dr \quad \text{(blade element)}$$

(2.6)

$C_{\theta,1}$ denotes the tangential velocity in the wake and is given as $2a'\omega r$ where ω is the angular velocity of the rotor blades and a' is the tangential induction factor and that by definition describes the tangential velocity of the air at the rotor plane induced by the torque from the rotor as, $C_\theta = a'\omega r$, and is just as the axial induction factor the mean of the upstream value 0 m/s and the wake value $2a'\omega r$. The tangential velocity at the rotor plane is also seen in Figure 2.2 and the direction is opposite the blade rotation since the induced wind is the reaction from the aerodynamic loads also shown in the Figure. From Figure 2.2 is seen that

$$V_{rel} = \frac{(1-a)V_o}{\sin\phi} \quad \text{and} \quad V_{rel} = \frac{(1+a')\omega r}{\cos\phi}$$

(2.7)

Combining Eqs. (2.5)-(2.7) an expression for the tangential induction factor is derived

$$a' = \cfrac{1}{\cfrac{4\sin\phi\cos\phi}{\sigma C_t} - 1}$$

(2.8)

Equations (2.4) and (2.8) express the non-dimensionalized axial and tangential induced velocities, respectively, as shown in Figure 2.2 when there is no azimuthal variations of the aerodynamic loads corresponding to a rotor with an infinite number of blades. Prandtl developed a correction to the aerodynamic loads, $C_{n,cor} = C_n / F$, so that when used in the momentum equations assuming infinite number of blades yields the induced velocities at the blades that would be present on a rotor having a finite number of blades. Prandtl's tip loss factor as also shown in more details in [3] is given by following expression

$$F = \frac{2}{\pi}\arccos(\exp(-\frac{B(R-r)}{2r\sin\phi}))$$

(2.9)

The formal derivation will not be given here, but later it will be shown that it is based on a simplified description of the wake behind the wind turbine rotor, and that it agrees very well with a numerical solution of a lifting line method applying a realistic trailed helical vortex system.

Introducing Prandtl's tip loss correction into the momentum equations yield two equations for a and a' that can be used to calculate at various radial positions the size and orientation of the relative wind to the rotor blades and further applying 2-D aerofoil data also the aerodynamic loads along the blades.

$$a = \cfrac{1}{\cfrac{4F\sin^2\phi}{\sigma C_n} + 1}$$

(2.10)

and

$$a' = \cfrac{1}{\cfrac{4F\sin\phi\cos\phi}{\sigma C_t} - 1}$$

(2.11)

Equation (2.10) assumes that the wake develops "smoothly" and that the streamlines are simply gradually expanding as sketched in Figure 2.1. However, if the thrust force becomes large compared to the momentum of the free wind there is a risk that the flow reverses and becomes unsteady and chaotic as sketched in Figure 2.3.
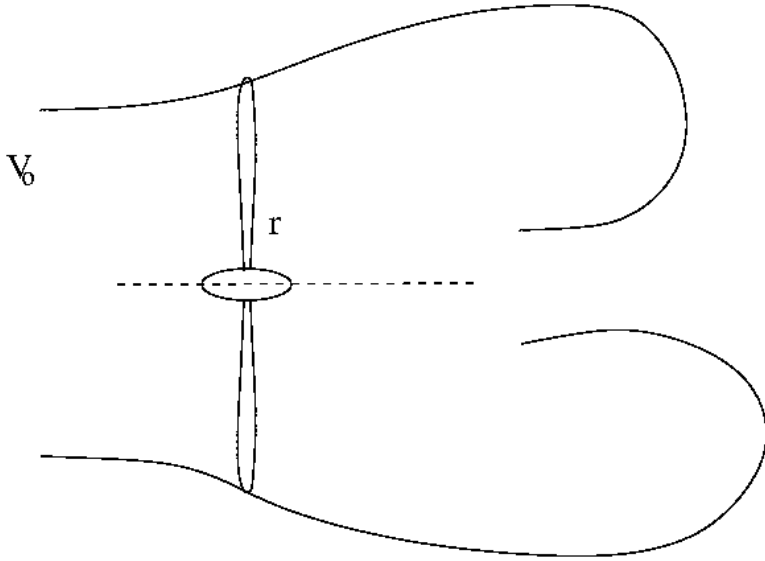

Figure 2.3: Sketch of the turbulent wake state for high values of C_T resulting in unsteady and reversed flow.

This situation is called the turbulent wake state and it is not possible to write a simple expression for the axial momentum equation as Eq. (2.1) and to overcome this in a simple way one can replace the momentum theory Eq. (1.14) by an empirical relationship between the thrust coefficient and the axial induction factor for large values of C_T as e.g.

$$C_T = 4Fa(1 - f_g a)$$

$$f_g = \begin{cases} 1 & a \leq \frac{1}{3} \\ \frac{1}{4}(5 - 3a) & a > \frac{1}{3} \end{cases}$$

(2.12)

An empirical relationship for $C_T(a)$ as the one given in Eq. (2.12) and shown graphically in Figure 2.4 is called a Glauert correction and different correlations can be found in the literature. Note that also Prandtl's tip loss correction has been included in Eq. (2.12) to correct for a finite number of blades.
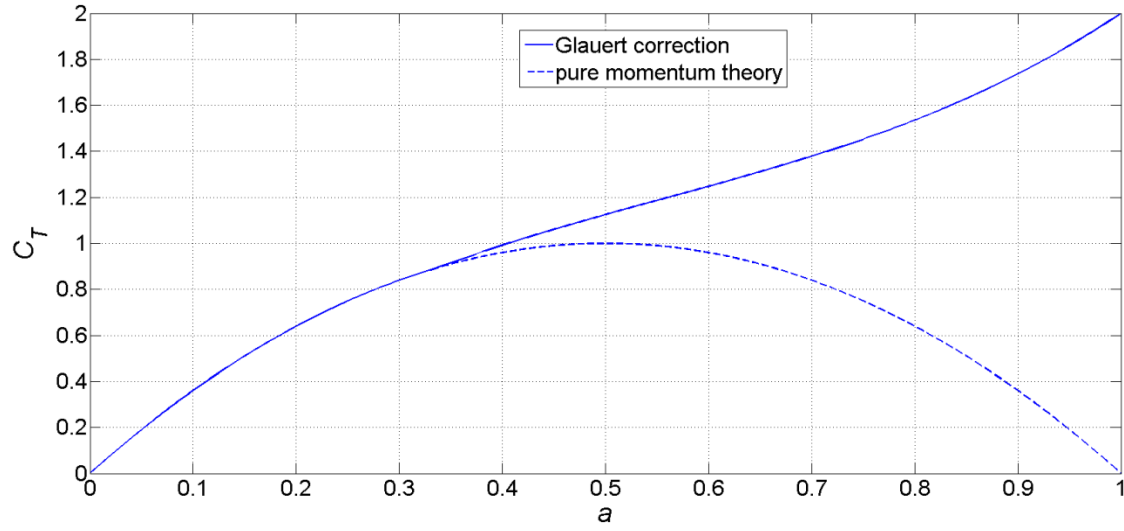
Figure 2.4: Empirical Glauert correction for $C_T(a)$ and compared to pure momentum theory

The definition of the thrust coefficient for an annular element of the rotor as the one shown in Figure 2.5 is

$$C_T = \frac{dT}{\frac{1}{2}\rho V_o^2 dA} = \frac{B\frac{1}{2}\rho V_{rel}^2 c C_n dr}{\frac{1}{2}\rho V_o^2 2\pi r dr} = \frac{\sigma C_n V_{rel}^2}{V_o^2} = \frac{\sigma C_n (1-a)^2}{\sin^2 \phi} \qquad (2.13)$$
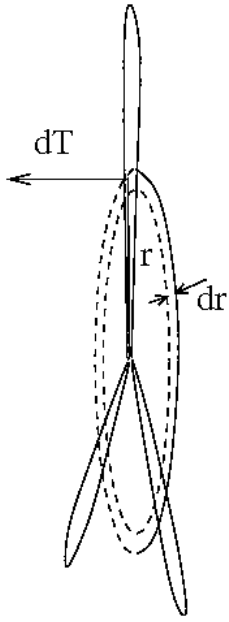
Figure 2.5: An annular ring locally in the rotor plane

If Eqs. (2.12) and (2.13) are combined it is seen that for $a<1/3$ the equation for a becomes equal to the previously derived Eq. (2.10), but for $a>1/3$ it is necessary to solve for the value of a that satisfies Eq. (2.13) and $C_T = 4Fa(1 - \frac{1}{4}(5 - 3a)a)$

The equations (2.10)-(2.13) can for a given rotor geometry, wind speed and rotational speed be solved at various radial positions to determine the induced wind and thus also give the length and position of the local relative wind speed, see Figure 2.2

$$V_{rel}^2(r) = (1-a)^2 V_o^2 + (1+a')^2 \omega^2 r^2$$
$$\tan\phi = \frac{(1-a)V_o}{(1+a')\omega r} \tag{2.15}$$

From the various aerofoils and their 2-D lift and drag coefficients the lift and drag are calculated from Eq. (2.2).

The angle of attack, α, is the difference between the flowangle, ϕ, and the angle of the aerofoil relative to the rotor plane, θ, as seen in Figure 2.2. The angle, $\theta(r)$, is a combination of the geometric twist of the blade,

$\beta(r)$ measured relative to the tip aerofoil and the pitch angle, θ_p, that is the angle of the tip aerofoil relative to the rotor plane as shown in Figure 2.6 and the angle of attack therefore becomes
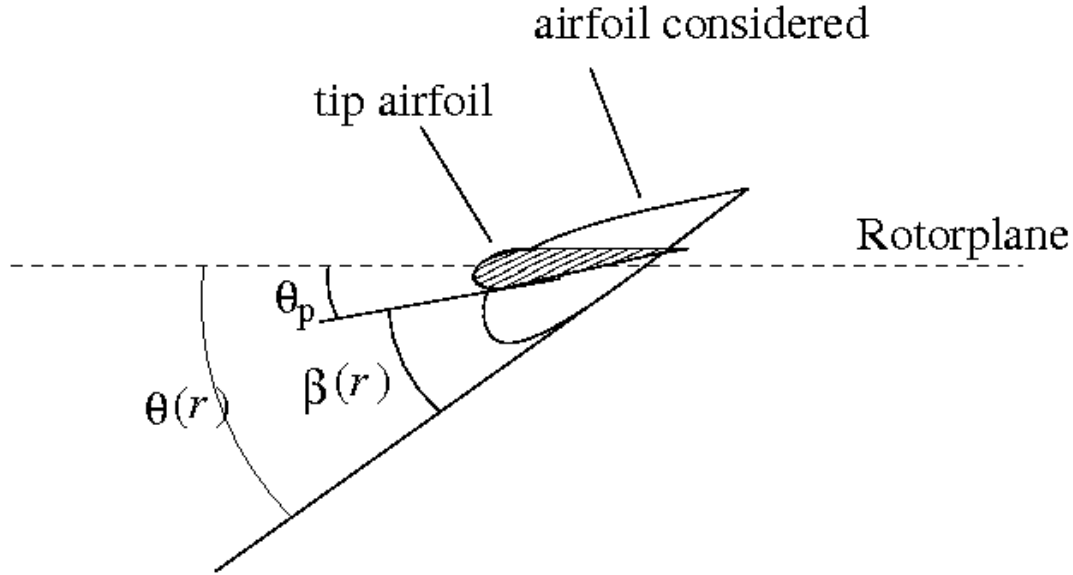

Figure 2.6: Angle of local aerofoil with rotor plane

$$\alpha(r) = \phi - (\theta_p + \beta(r)) \tag{2.16}$$

The aerodynamic lift and drag distributions can be projected normal and tangential to the rotor plane and integrated to determine the thrust, torque and power as

$$T(V_o, \omega, \theta_p) = B \int_0^R (l \cos \phi + d \sin \phi) dr \tag{2.17}$$

$$M(V_o, \omega, \theta_p) = B \int_0^R r(l \sin \phi - d \cos \phi) dr \tag{2.18}$$

$$P(V_o, \omega, \theta_p) = \omega \cdot M(V_o, \omega, \theta_p) \tag{2.19}$$

3. Unsteady BEM

The equations in section 2 can be used to calculate the steady load distributions, the overall thrust and power for a given wind turbine for various wind speeds, rotational speeds and pitch angles and may thus be used in a rotor design process. A wind turbine that is operating under free atmospheric conditions experiences, however, a spatially and temporarily varying wind speed due to mainly wind shear, atmospheric turbulence and yaw misalignment so that the wind velocity, V_o, in the velocity triangle Figure 2.2 in every section is constantly changing in time giving rise to unsteady loads that will cause dynamic deflections and fatigue loads. Provided that a realistic turbulent wind speed can be described as time series in a discrete number of points covering the rotor area, as shown in Figure 3.1, these can at each time be interpolated to the position of a blade element and used as input to the velocity triangle.
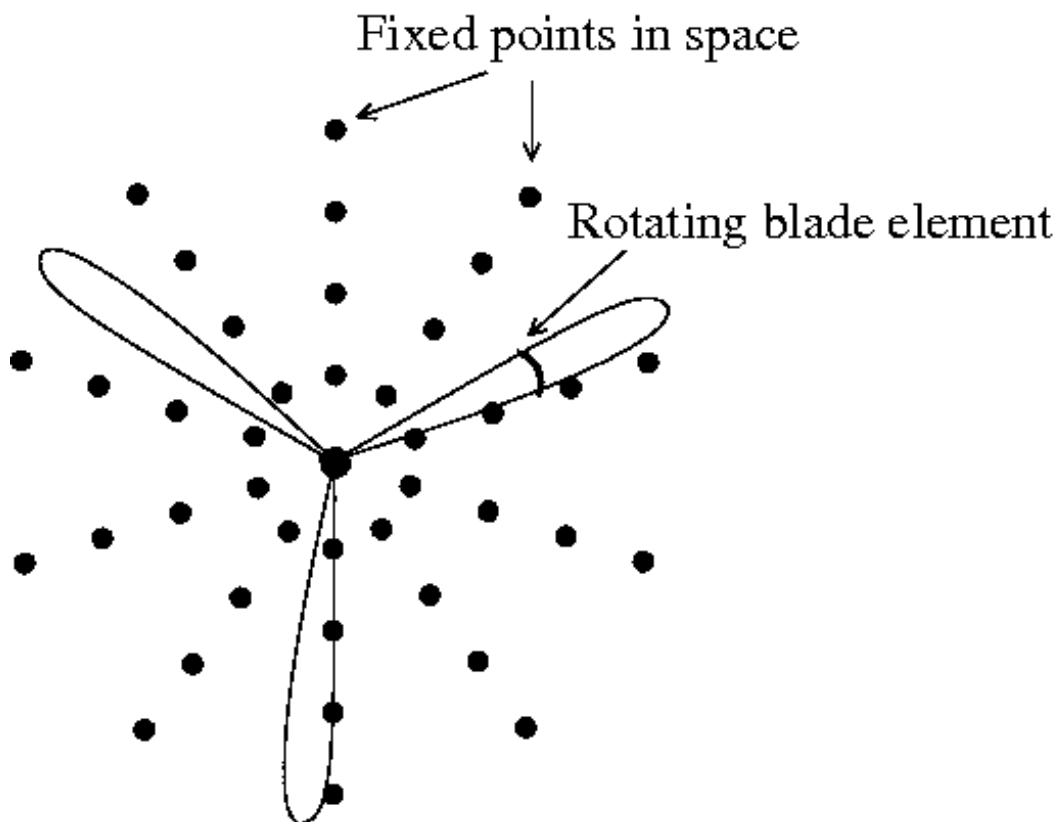

Figure 3.1: Sketch of grid for storing spatially correlated wind time series.

Two different methods often used to determine spatially correlated time series and having a prescribed Power Spectral Density function are referred to as the Veers method [5] and the Mann model [6].

The classical BEM equations as presented in section 2 must be extended to take the response time of the induced wind to a change in loading into account in order to calculate correctly the time dependent aerodynamic loads. The steady equations for the axial and tangential induction factors can be rewritten to Eqs. (3.1) and (3.2) to calculate directly the quasi steady axial and tangential induction velocities in a coordinate system following the rotor plane as shown in 3.2.
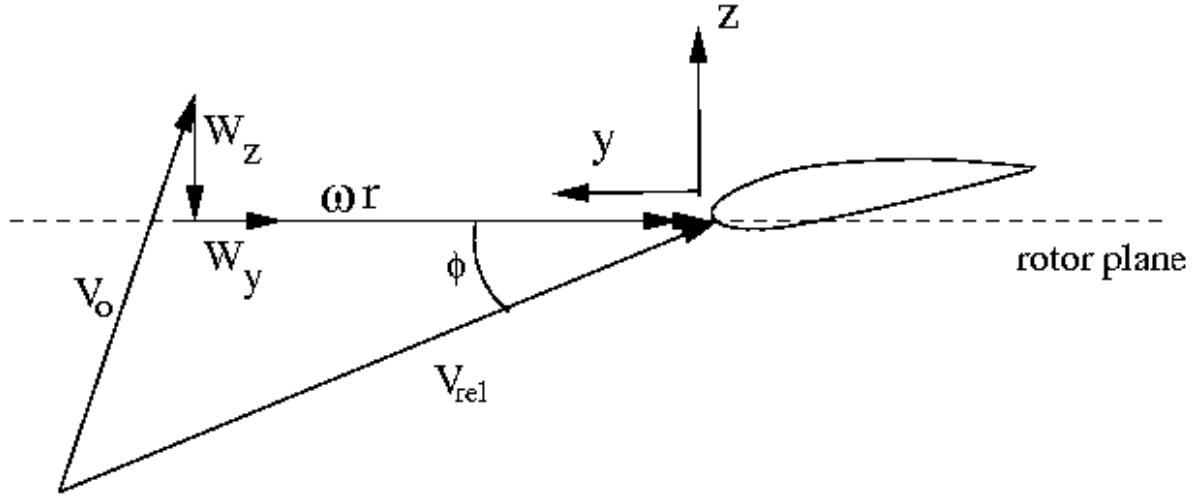

Figure 3.2: Blade coordinate system

$$W_z^{qs} = \frac{-Bl\cos\phi}{4F\rho\pi r\sqrt{V_{o,y}^2 + (V_{o,z} + f_g W_z)^2}}$$ (3.1)

$$W_y^{qs} = \frac{-Bl\sin\phi}{4F\rho\pi r\sqrt{V_{o,y}^2 + (V_{o,z} + f_g W_z)^2}}$$ (3.2)

The quasi steady induced velocities in Eqs. (3.1) and (3.2) express the induced wind that is in equilibrium with the lift and are for zero yaw misalignment identical to Eqs. (2.10) and (2.11). Also the equations (3.1) and (3.2) are consistent with momentum theory for helicopters similar to a wind turbine at 90° yaw, and it is without any proof therefore assumed that they are also valid between 0 and 90° yaw misalignment. At any new time the approaching wind speed for a blade element is changed both in size and direction and further the pitch angle may have been altered from the previous time by the control system. The quasi steady induced wind corresponding to the modified lift associated with this new angle of attack can be computed from Eqs. (3.1)

and (3.2) but due to the large inertia of the approaching wind there is a long response time to reach this equilibrium value, and in practice this time delay may be simulated using a time filter as e.g. the one proposed by Øye, see [7]

$$W_{\text{int}} + \tau_1 \frac{dW_{\text{int}}}{dt} = W^{qs} + 0.6\tau_1 \frac{dW^{qs}}{dt}$$

$$\tau_1 = \frac{1.1}{1-1.3a} \cdot \frac{R}{V_o}$$

(3.3)

$$W + \tau_2 \frac{dW}{dt} = W_{\text{int}}$$

$$\tau_2 = (0.39 - 0.26 \cdot \left(\frac{r}{R}\right)^2)\tau_1$$

(3.4)

The two time constants, τ_1, and τ_2 in the Øye dynamic inflow model are calibrated using a vortex model, where τ_1, represents a convective time in the order of the time it takes an air particle to move between one and two rotor radius, R, with the free wind speed, V_o. The time constant τ_2 models the radial dependency, so that the elements near the tip reacts faster than the more inboard ones. It should be noted that when using Eq. (3.3) to calculate τ_1 the axial induction factor, a, should be limited to not exceed 0.5. The two differential equations Eqs. (3.3) and (3.4) can be solved analytically if the right hand sides are kept constant. First, an intermediate induced wind speed is found solving Eq. (3.3) using the time constant τ_1 and quasi steady values as input to the first order differential equation. Next, the final filtered value is found solving a similar differential equation (3.4) but now using time constant τ_2 and the intermediate value as input. The solution to Eqs. (3.3) and (3.4) simulates realistically the time delay to reach the steady solution that changes in every time step. When solving in the time domain Eqs. (3.1) and (3.2) for the quasi steady induced wind one may utilize that the induced wind due to the time filter Eqs. (3.3) and (3.4) changes very little in one time step, since a typical time step is much smaller than τ_1, and τ_2, and simply apply old values for the induced wind when estimating the right hand side. In reference [7] alternatives to the Øye time delay models are shown

The unsteady BEM runs in the time domain and the algorithm can be described as:

Initialize pitch, rotor speed, rotor azimuth position and pre calculate realistic and spatially correlated time histories of the approaching wind in the rotor plane.

Then for each time step

    Update rotor azimuth position

    For each blade element

        Determine approaching wind speed using spatial and temporal interpolation

        Solve for quasi steady induced wind Eqs. (3.1) and (3.2)

        Apply the dynamic wake filter Eqs. (3.3) and (3.4) to determine the actual induced wind

        Determine the size and position of the relative wind speed, see velocity triangle Fig. 3.2

        Calculate using 2-D airfoil data the lift and drag, Eqs. (2.2)

    End element loop

    Integrate the spanwise loading to determine thrust, power and bending moments

    Optional: Call controller to update pitch and rotor speed

End time loop

To see the effect of the dynamic inflow model a simplified simulation is made for the 2 MW Tjaereborg wind turbine as described in [8] and where the rotor speed and wind speed are kept constant at ω=2.3 rad/s and V_o=10m/s, respectively. A prescribed pitch motion (step function) is enforced as shown in Figure 3.3. Figures 3.4 and 3.5 depict, respectively, the responding power and the induced wind normal to the rotor plane, W_z at 80 % span.
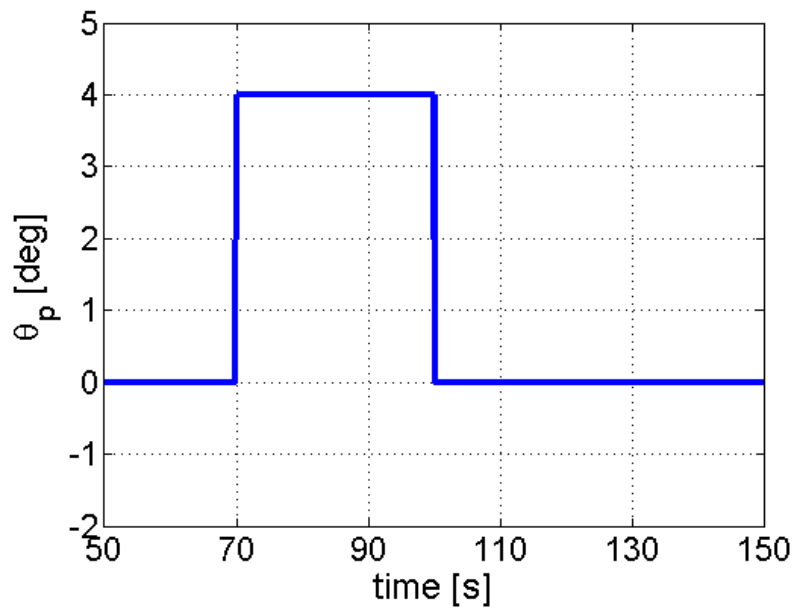
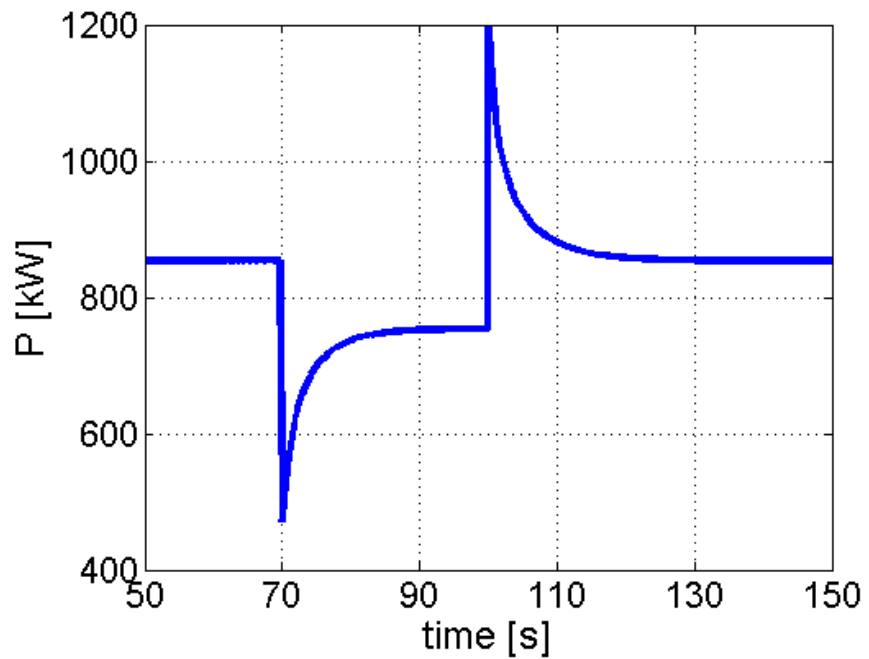Figure 3.3: Forced pitch motion (step input) used in BEM simulation

Figure 3.4: Computed power response for a step input in pitch angle as shown in Figure 3.3 for the 2MW Tjaereborg wind turbine [8], V_o=10 m/s and ω=2.3 rad/s
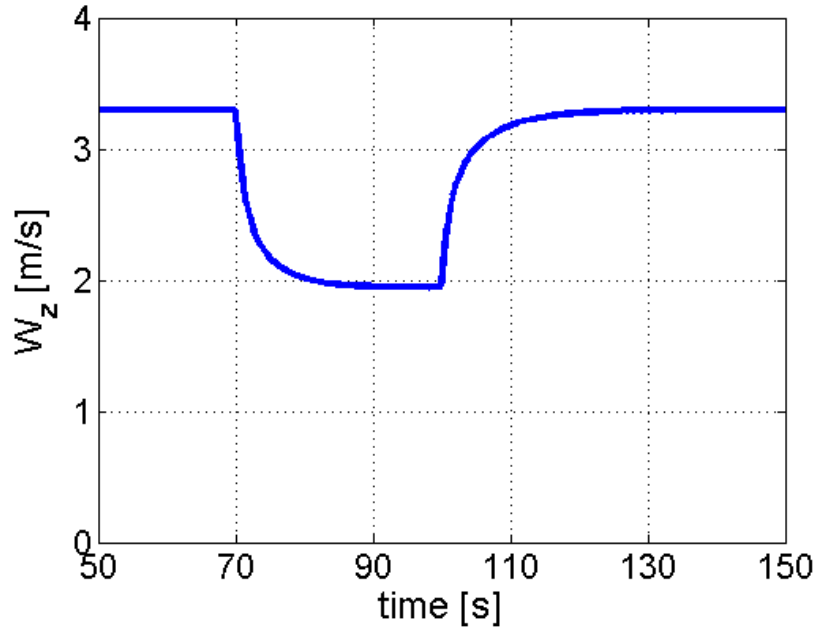
Figure 3.5: Computed time history of the induced wind normal to rotor at r/R=0.8 for a step input in pitch angle as shown in Figure 3.3 for the 2MW Tjaereborg wind turbine [8], V_o=10 m/s and ω=2.3 rad/s

 As the pitch is suddenly increased at t=70 s the angle of attack immediately drops, see Eq. (2.16). The aerodynamic lift decreases with the lowered angle of attack giving the sharp drop in power at t=70 s as also seen in Figure 3.4. Just after the pitch step the induced wind is no longer in equilibrium with the lowered lift and the gradual recovery towards a new and lower equilibrium induced wind calculated with the dynamic wake filter Eqs. (3.3) and (3.4) is plotted in Figure 3.5. It is seen that it takes several seconds to reach this new equilibrium and that the power slowly increases from the undershoot value just after the pitch step as the induced wind is gradually lowered by the decreased lift. At t=100 s the pitch is forced back to 0° and an overshoot in power is observed until the induced velocity and power has adapted to the new increased lift. Also one should apply a time filter for the 2-D steady lift and drag coefficients, since the aerodynamic loads do also not respond immediately to a change in angle of attack, but at a much faster rate than the dynamic wake model. Two examples of dynamic stall models often used for wind turbines are the Øye model [9] and the Beddoes-Leishman model [10] and [11].

Figure 3.6 and 3.7 present simulated time series using the unsteady BEM method for power and normal load at 80% span for the Tjaereborg rotor operating at a constant angular velocity ω=2.3 rad/s, pitch=0° and a temporally and spatially varying turbulent wind speed calculated using the Veers method [4] for a Kaimal spectrum (I=10% , $V_{o,mean}$=10 m/s and L=600 m) and a coherence function depending on the frequency, f, and distance between two points, d, as

$$coh(f,d) = \exp(-\frac{12 f \cdot d}{V_o})$$
(3.5)

The coherence function ensures a realistic spatial distribution so that the time histories of two points become closer correlated when the distance, d, between them are decreased. Further, the correlation also depends on the frequency which together with the wind speed represents the size of the approaching turbulent eddies, so that the large turbulent structures, corresponding to low frequencies, increases the spatial correlation between points having a distance smaller than the size of the turbulent structures.
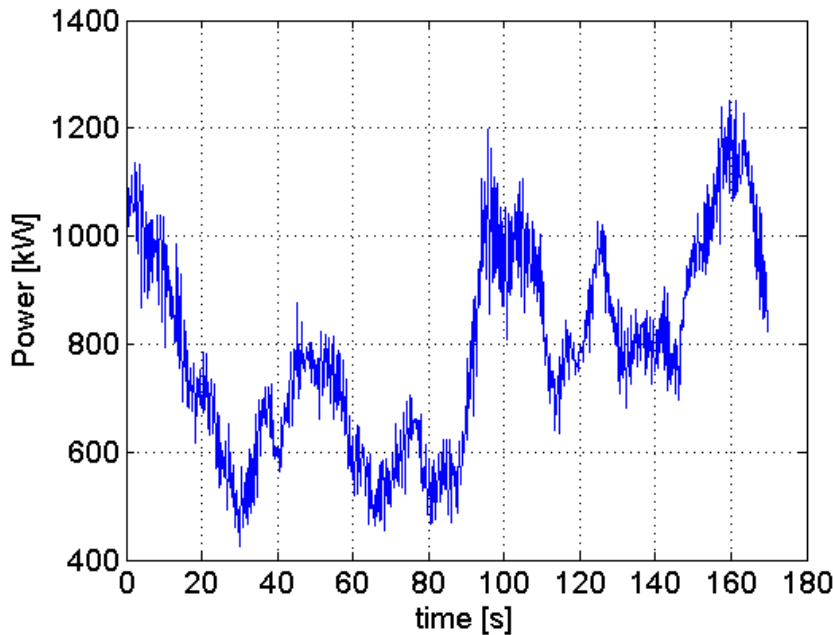

Figure 3.6: Computed time series of mechanical power for the 2MW Tjaereborg wind turbine [8], ω=2.3 rad/s, θ_p=0° and simulated turbulent inflow based on a Kaimal spectrum (I=10% , $V_{o,mean}$=10 m/s and L=600 m)
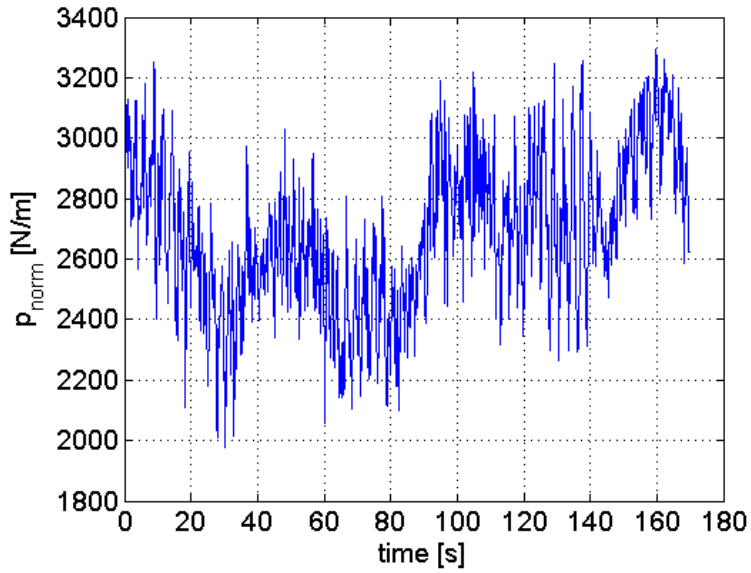
Figure 3.7: Computed time series of blade load normal to the rotor at radial position r/R=0.8 for the 2MW Tjaereborg wind turbine [8], ω=2.3 rad/s, θ_p=0° and simulated turbulent inflow based on a Kaimal spectrum (I=10% , $V_{o,mean}$=10 m/s and L=600 m)

In Figure 3.8 the Fourier transform of the time series for the normal load at the spanwise position r/R=0.8 from Figure 3.7 is plotted and it is seen that there is strong content at the rotational speed of the rotor.
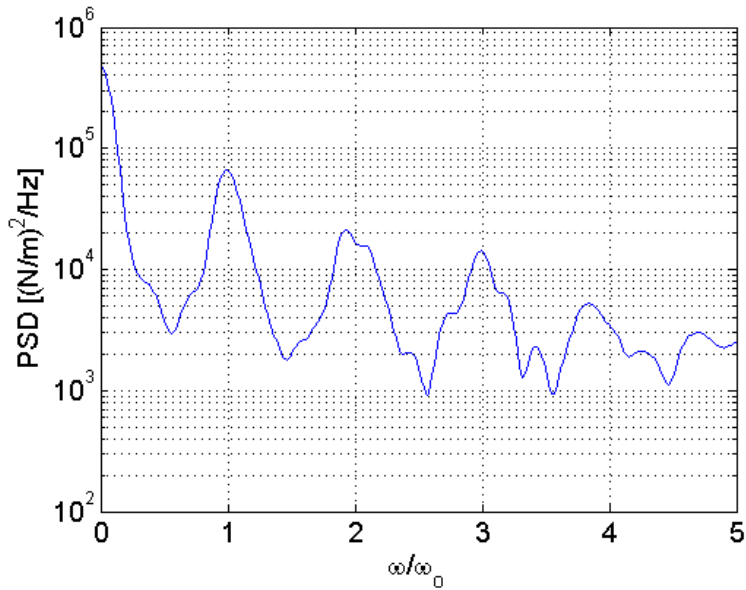
Figure 3.8: Fourier transform of the blade normal load time history shown in Figure 3.7. The frequencies are non-dimensionalized with the rotor speed ω_o=2.3 rad/s.

  This is because the large turbulent structures remain inside the rotor plane for several revolutions and a blade thus goes through these once per revolution and the angular speed of the rotor is often denoted 1P for once per revolution. Also there is seen spikes at 2P, 3P etc., but these are harmonics to the 1P variation. Figure 3.9 shows the Fourier transform of the power time history from Figure 3.6 and here is seen that the 1P and 2P frequencies have disappeared and the reason being that the time histories of the tangential load for blade number 2 and 3 are phase shifted 120 and 240 degrees, respectively, relative to blade number 1 and when the 1P and 2P components for all three blades are added the result becomes constant. However, the 3P and 6P components become in-phase and add up to a spike. Another very important contribution to 1P aerodynamic load variations is wind shear, where a blade sees a higher wind speed when pointing upwards than half a revolution later when it is pointing downwards and thus closer to ground. This 1P variation in apparent wind speed influences directly the angle of attack and thus the aerodynamic loads.
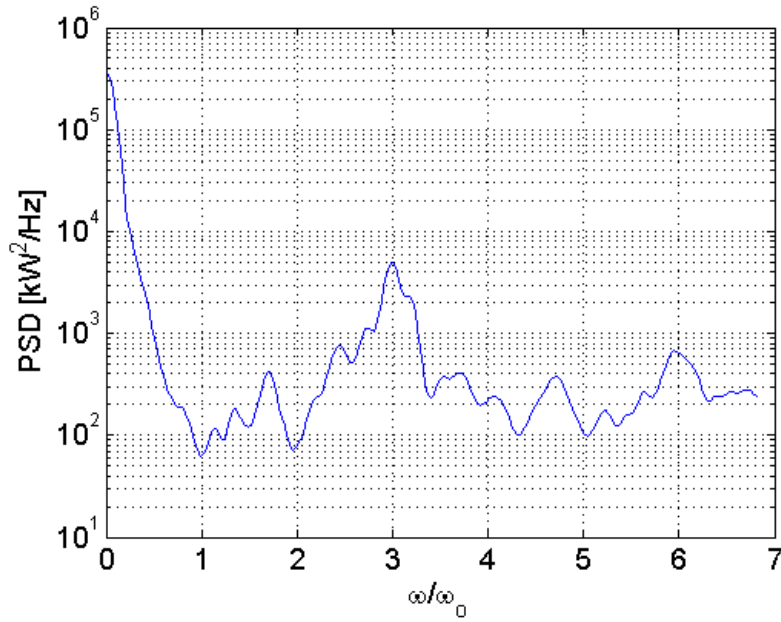
Figure 3.9: Fourier transform of the power time history shown in Figure 3.6. The frequencies are non-dimensionalized with the rotor speed ω_o=2.3 rad/s.

Understanding the frequency responses is important when designing the structure in order to avoid amplified vibrations from resonance.

4. Lifting line model and explaining Prandtl's tip loss correction

The aerodynamics of a wind turbine rotor may also be explained and quantified using an extended lifting line model, which is similar to the classical Prandtl's lifting line model for a translating wing and where the only difference lies in the wake geometry behind the wing. The lifting line theory is essentially a vortex theory where the local lift creates a bound circulation on the blade that may be computed from the Kutta-Joukowski theorem as

$$l = \rho V_{rel} \Gamma \tag{4.1}$$

The lift in Eq. (4.1) is perpendicular to the incoming flow and the circulation is oriented along the blade as shown in Fig. 4.1.
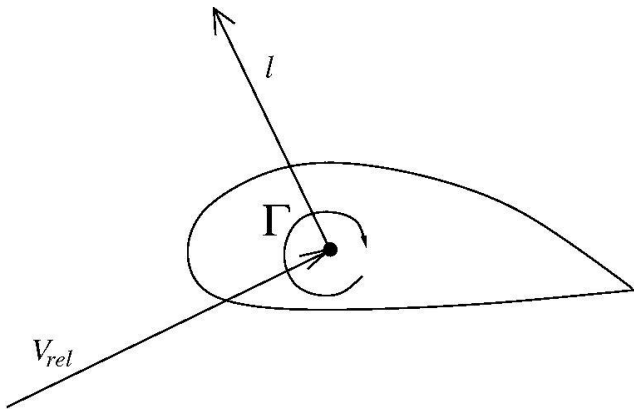
Figure 4.1: Kutta-Joukowsky theorem showing the relationship between lift, inflow and circulation for a 2-D airfoil.

When the lift and thus the circulation on a 3-D wing is varying along the span a vortex with the strength determined by the spanwise gradient is trailed in the wake behind the blade and moves with the flow in order to fulfil Helmholz theorem stating that a vortex line cannot end in a fluid. In a discrete model where the blade is considered to be divided in sections with constant circulation the Helmholz theorem can be achieved if the circulation from each section is trailed in the wake as helical horseshoe vortices as shown in a 2-D sketch in Fig. 4.2.
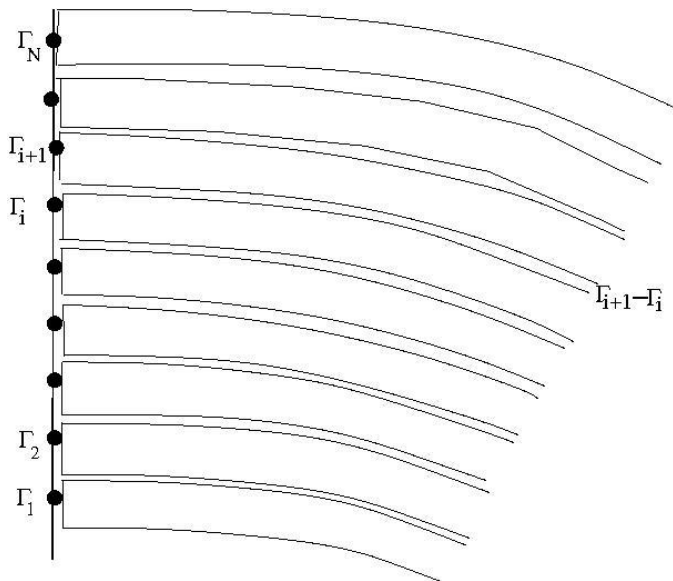

Figure 4.2: Discrete lifting line model for a wind turbine blade. The trailed streamlines are in this drawing cut of after some distance behind the blade

The trailed vortex lines drawn in Fig. 4.2 are cut off, but they should continue to infinity in a helical geometry as shown in 3-D in Figure 4.3.
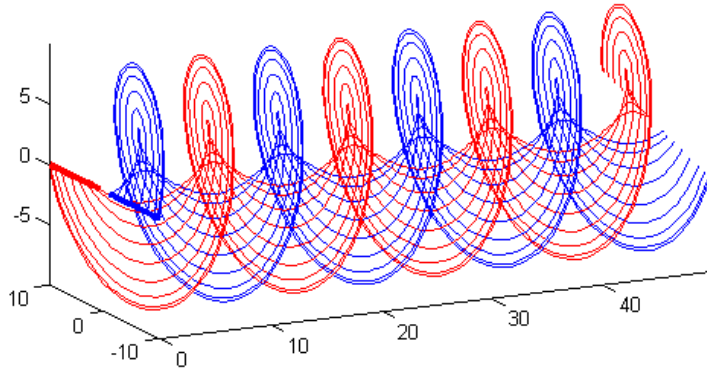

Fig 4.3: 3-D plot of the discrete trailing vortices behind 2-bladed rotor

Next if the strength, Γ, of a vortex line and its position in space is known the velocity induced in any spatial point can be computed from the Biot-Savart law as (see also Figure 4.4 for more explanation)

$$\mathbf{dW} = \frac{\Gamma}{4\pi} \int_A^B \frac{\mathbf{ds} \times \mathbf{r}}{|\mathbf{r}|^3}$$
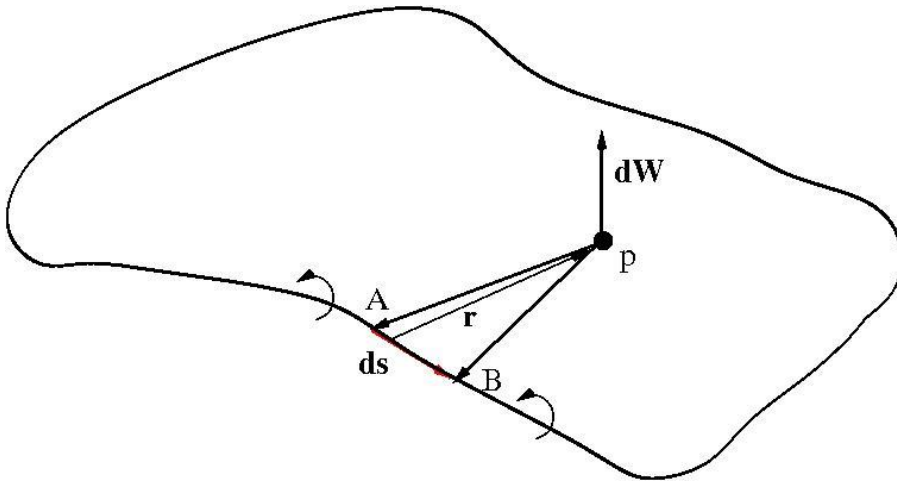
$$\mathbf{W} = \oint \mathbf{dW}$$

(4.2)

Fig4.4: Integration of Biot-Savart law to determine induced velocity in point p in space from closed vortex line with strength Γ.

If the pitch of the helical vortices and their strength are known it is possible to compute the induced wind on the rotor blades, but it is also possible to calculate the radial distribution along the blades that will result in a constant axial induced wind speed on the blades. A rotor with a constant induced wind speed will also give that the helical pitch is constant with the radius and Betz proved that this is the distribution that minimizes induced drag. With such a model it is possible to compute numerically and compare this optimum circulation distribution for various numbers of blades. Such a calculation is made for a rotor with a radius of R=10 m, a wind speed of 9 m/s, a tip speed ratio $\lambda=\omega R/V_o$=7 and an axial induction factor a=0.333 corresponding to an induced wind in the rotor plane of 3 m/s and the resulting circulation distributions are shown in Figure 4.5 for different number of blades (B=1,3,6 and 18) and it is observed that the radial distribution of circulation becomes more and more constant with increasing number of blades. In Figure 4.6 is shown Prandtl's tip loss correction, Eq. (2.9) and the ratio between the circulation for B=3 and B=18, where the one having 18 blades is considered to represent an infinite number of blades. It is seen that Eq. (2.9) represents quite well the ratio between the circulation distribution for a finite number of blades and an infinite number of blades resulting in a constant induction. And this is exactly the situation that Prandtl tried to solve using potential flow theory but had to assume a simplified wake to represent the real helical shape as shown in Fig. 4.3. The ratio between the circulations can using Eq. (4.1) be interpreted as the ratio between the lift distribution on a finite number of blades and infinite number of blades resulting in a constant induction

$$\frac{l_B}{l_\infty} = \frac{\Gamma_B}{\Gamma_\infty} = F \Rightarrow l_\infty = \frac{l_B}{F} \tag{4.3}$$

When setting up the momentum equations in the Blade Element Momentum model an infinite number of blades was assumed, but the lift in the Blade Element part is evaluated at the blades as l_B, so the loads to use in the momentum part is estimated using Eq. (4.3) eventually leading to Eqs. (2.10) and (2.11).
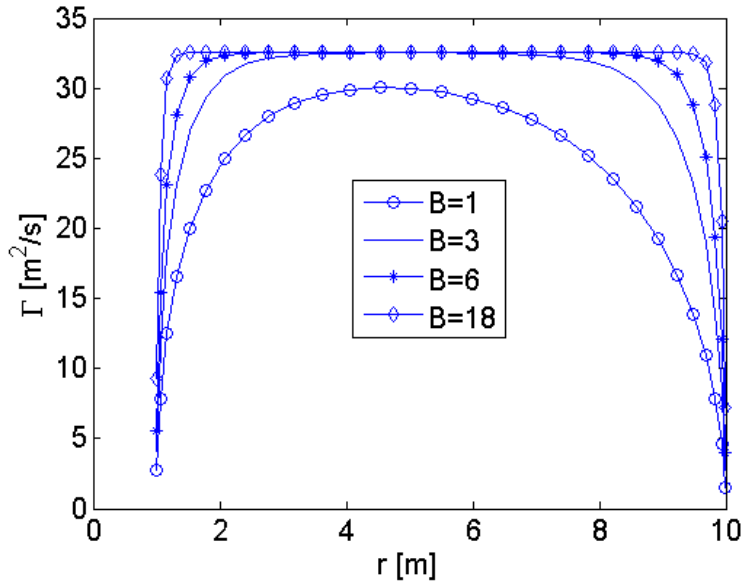

Fig4.5: The distribution of circulation that gives a constant induced velocity of 3 m/s for a rotor having a radius of R=10m, a wind speed of 9 m/s and a tip speed ratio $\lambda=\omega R/V_o=7$
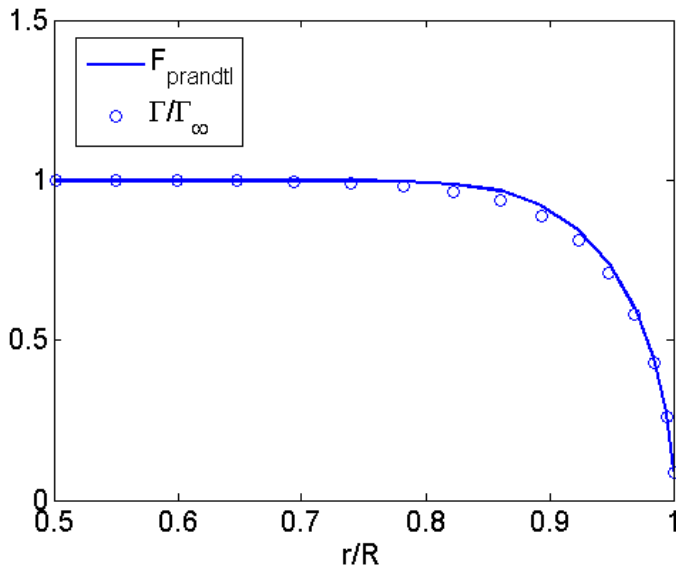

Fig4.6: Prandtl's tip loss correction and the ratio between the circulation distribution for a finite number of blades and an infinite number of blades as function of radius.

5. Limitations to the simpler aerodynamic models

At the same time as trying to explain the basics behind the power production from a wind turbine rotor also the simple but widely used BEM method is presented. To do a full load validation as e.g. described in the standards such as IEC 64300-1 [12] more than 1000 load cases have to be computed for a land based wind turbine and even more offshore. Each load case consists of time series, typically 10 minutes using a time increment in the order of 0.1s, demanding the aerodynamic loads to be computed many times and a fast algorithm is needed and BEM is therefore still the workhorse for load validations. For normal operations where the flow is mostly attached to the blade surface the BEM method as described in sections 2 and 3 gives very good agreement with measurements validating the use of local 2-D airfoil data and the assumption of the elements being independent. However, at high angles of attack as e.g. experienced by stall regulated wind turbines the agreement is not always perfect and one may cure this by correcting the lift and drag coefficients to account for 3D effects in a separated and rotating boundary layer. In [13] one method is proposed to increase the lift in stall by adding an extra term that is proportional to the difference in the actual 2D lift data and the lift coefficient for the non-separated flow. Further the added lift is also multiplied by the ratio between the local chord and the radial position as shown in Eq. (5.1), so that the 3D effect diminishes with increased radius. In [14] a similar expression is proposed, but where the added lift is multiplied with the square of the ratio between the local chord and the radial position. But in both cases the term ΔC_l keeps increasing with the angle of attack and thus corrections as proposed in [13] and [14] should not be used in deep stall where the lift coefficient is assumed to again be the uncorrected and equal to the 2D value since otherwise unrealistic high values would be achieved.

$$C_{l,3D}(\alpha) = C_{l,2D}(\alpha) + 2.2 \cdot \left(\frac{c}{r}\right) \cdot \Delta C_l(\alpha)$$

$$\Delta C_l = C_{l,inv} - C_{l,2D}$$

(5.1)

Also the assumption of spanwise independent flow may not hold when using aerodynamic devises such as a flap that can give locally strong spanwise gradients in the lift and that will shed trailing vortices as described in the lifting line model in section 4 that affect the neighbouring inflow angles. Also a separation starting at the root where the angles of attack are highest and where thick aerofoils are used may spread further outboard again violating the assumption that each blade element can be considered independent. To overcome this one may use a more advanced aerodynamic models such as 3D panel methods strongly coupled to the viscous boundary layer equations, see e.g. [15]-[17]. The ultimate aerodynamic model is to solve the full Navier-Stokes equations for the flow past a wind turbine rotor and where the loads can be computed from the pressure and skin-friction distribution on the rotating blades. There has been a tremendous improvement of using these models to validate rotor designs and a whole chapter in this book is therefore devoted to this. Finally, also the so called Actuator Line, AL, model as first described in [18] has become very popular, especially for studying the flow in wind farms and should therefore also be briefly mentioned. Basically it is a Blade Element model where

the aerodynamic loads are computed from the velocity triangular as drawn in Figure 3.2 and 2D airfoil data, but instead of using the momentum theory as in BEM to compute the induced flow one uses CFD, where the aerodynamic loads in each time step is introduced as body forces along the blade positions and their reaction to the inflow is determined from solving the Navier-Stokes equations.

References:

[1] Froude RE. On the part played in propulsion by difference in pressure. Transaction of the Institute of Naval Architects, 1889; 30: 390–423.

[2] Rankine, WJM. On the mechnical principles of the action of propellers. Transaction of the Institute of Naval Architects, 1865; 6: 13–39.

[3] Glauert, H. *Airplane Propellers* from Aerodynamic Theory, vol. 4, Division L edited by Durand W.F., pp. 169-360

[4] Drzewiecki S. (1892) 'Bulletin de l'Association Technique Maritime'

[5] Veers, P. (1988) 'Three-Dimensional Wind Simulation' SANDIA REPORT, SAND88-0152 UC-261

[6] Mann J. (1998) 'Wind field simulation', Problems in Engineering Mechanics, vol. 13, pp269-282

[7] Snel H and Schepers JG (1995) Joint Investigation of Dynamic Inflow Effects and Implementation of in Engineering Method, ECN-C- -94-107.

[8] Hau E., Langenbrinck J., Palz W. (1993), WEGA Large Wind Turbines, Springer

[9] Øye S (1991) 'Dynamic Stall, simulated as a time lag of separation' in McAnulty (ed) Proc. 4th IEA Symposium on the Aerodynamics of Wind Turbines, ETSU-N-118

[10] Leishman JG and Beddoes TS (1989) 'A Semi-Empirical Model for Dynamic Stall' *Journal of the American Helicopter Society*, 34(3) pp 3-17

[11] Hansen MH, Gaunaa M and Madsen HA (2004) 'A Beddoes-Leishman type dynamic stall model in state-space and indicial formulations' Risoe-R-1354(EN)

[12] IEC 61400-1:2005+AMD1:2010 Design requirements

[13] Chaviarropoulos P.K. and Hansen M.O.L., 'Investigating Three-Dimensional and Rotational Effects on Wind Turbine Blades by Means of a Quaso-3D Navier-Stokes Solver, Journal of Fluids Engineering, Vol. 122, pp. 330-336, 2000

[14] Snel H, Houwink B, Bosschers J, Piers WJ, van Bussel GJW, Bruining A (1993) 'Sectional prediction of 3-D effects for stalled flow on rotating blades and comparison with measurements' in proceedings *ECWEC 1993*, pp 395-399.

[15] Ramos-García N., Sørensen J.N. and Shen W.Z., A Strong Viscous-Inviscid Interaction Model for Rotating Airfoils. Wind Energy, Volume 17, Issue: 1, pages: 1957-1984, 2014

[16] Ramos-García N., Sørensen J.N. and Shen W.Z., Validation of a three-dimensional viscous-inviscid interactive solver for wind turbine rotors. Renewable Energy: Special Issue in Wind Energy Systems and Wakes. Volume 70, pages:78-92, October 2014.

[17] Ramos-García N., Sørensen J.N. and Shen W.Z., Three-Dimensional Viscous-Inviscid Coupling Method for Wind turbine Computations. Wind Energy, Volume 19, Issue 1, Pages 67-93, January 2016.

[18] Sørensen JN, Shen WZ. 2002. Numerical modelling of wind turbine wakes. J. Fluids Eng. 124, 393–399